

Thermodynamic and dynamical signatures of a quantum spin-Hall insulator to superconductor transition

Martin Hohenadler,^{1,2,*} Yuhai Liu,^{3,*} Toshihiro Sato,^{1,*} Zhenjiu Wang,^{1,4} Wenan Guo,^{5,3} and Fakhre F. Assaad^{1,6,†}

¹*Institut für Theoretische Physik und Astrophysik, Universität Würzburg, 97074 Würzburg, Germany*

²*Independent Researcher, Josef-Retzer-Str. 7, 81241 Munich, Germany*

³*Beijing Computational Science Research Center, 10 East Xibeiwang Road, Beijing 100193, China*

⁴*Max Planck Institute for the Physics of Complex Systems, Nöthnitzerstr. 38, 01187 Dresden, Germany*

⁵*Department of Physics, Beijing Normal University, Beijing 100875, China*

⁶*Würzburg-Dresden Cluster of Excellence ct.qmat, Am Hubland, 97074 Würzburg, Germany*

Thermodynamic and dynamical properties of a model of Dirac fermions with a deconfined quantum critical point (DQCP) separating an interaction-generated quantum spin-Hall insulator from an s-wave superconductor [Nature Comm. **10**, 2658 (2019)] are studied by quantum Monte Carlo simulations. Inside the deconfined quantum critical region bound by the single-particle gap, spinons and spinless charge-2e skyrmions emerge. Since the model conserves total spin and charge, and has a single length scale, these excitations lead to a characteristic linear temperature dependence of the uniform spin and charge susceptibilities. At the DQCP, the order parameter dynamic structure factors show remarkable similarities that support emergent Lorentz symmetry. Above a critical temperature, superconductivity is destroyed by the proliferation of spin-1/2 vortices.

I. INTRODUCTION

Phase transitions involving spontaneous symmetry breaking are a central topic of condensed matter physics. Zero-temperature ($T = 0$) *quantum phase transitions* [1], driven purely by quantum fluctuations, are particularly interesting. The tuning of external parameters such as pressure in their experimental realization can be thought of as changing the relative strength of different terms in the relevant microscopic Hamiltonian or field theory, thereby favoring distinct ground states above and below a critical value λ_c . While theoretical approaches often focus on $T = 0$, experiments rely on the finite-temperature signatures of such quantum critical points (QCPs) [2]. In the quantum critical region $k_B T > \Delta$, where $\Delta \sim \xi^{-z} \sim |\lambda - \lambda_c|^{z\nu}$ is a $T = 0$ energy scale and z, ν are critical exponents, quantum *and* thermal fluctuations play a crucial role [1].

Deconfined QCPs (DQCPs) [3, 4] separate two phases with different order parameters. The paradigmatic example is the transition from an antiferromagnet (AFM) to a valence bond solid (VBS). Within a Ginzburg-Landau description, a continuous transition between two different orders requires fine tuning. Otherwise, either a coexistence region or a first-order transition is expected. The CP¹ theory of DQCPs [3, 4], provides a generic mechanism for a continuous transition by means of topological defects of the order parameters. Vortex defects of the VBS order parameter carry spin-1/2. These spinons are the fundamental emergent quantity of the theory. At the critical point, they are deconfined and form a U(1) spin liquid [5]. The AFM phase arises from spinon condensation. In contrast, in the VBS phase, the spinons are gapped and VBS order is associated with the condensation of monopoles of the gauge field [6]. The latter are equivalent to skyrmions of the AFM order parameter and carry C_4 charge.

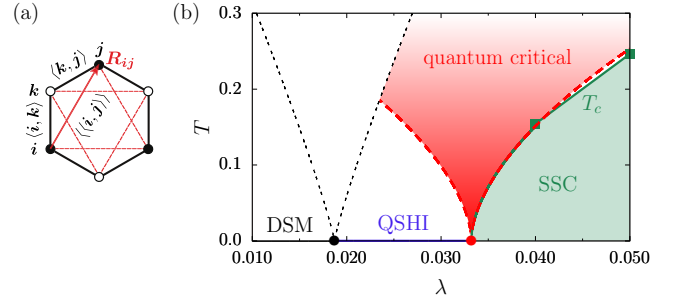


FIG. 1. (a) Notation in Eq. (1). (b) Phase diagram of Hamiltonian (1). Two quantum critical points at $\lambda_{c1} = 0.0187(2)$ [Dirac semimetal (DSM) to quantum spin Hall insulator (QSHI)] and $\lambda_{c2} = 0.0332(2)$ [QSHI to s-wave superconductor (SSC)] were established in Refs. [7, 8]. The DQCP quantum critical region is shown above $T = 5.35|\lambda - \lambda_{c2}|^{z\nu}$ (red dashed lines, $z = 1, \nu = 0.58$, prefactor obtained using $T_c(\lambda = 0.04) \approx 1/6.5$) and to the right of the crossover temperature scale $30.7|\lambda - \lambda_{c1}|^{z\nu}$ associated with the DSM-QSHI QCP (black dashed lines, $z = 1, \nu = 1/1.14$ [7], prefactor from $\Delta_{sp}(\lambda = 0.026) \approx 0.41$). The curve for $T_c(\lambda)$ corresponds to $5.35|\lambda - \lambda_{c2}|^{z\nu}$ for $\lambda \leq 0.04$ and a straight line for $\lambda > 0.04$.

Here, we investigate finite-temperature as well as spectral signatures of a DQCP within a recently introduced fermionic model [7] whose phase diagram is shown in Fig. 1(b). It describes interacting Dirac fermions in 2+1 dimensions and can be studied by quantum Monte Carlo (QMC) simulations without a sign problem. The DQCP separates an interaction-generated quantum spin-Hall insulator (QSHI) from an s-wave superconductor (SSC). Whereas the field theory description of the DQCP is based on an $SO(3) \times U(1)$ symmetry, the U(1) component is merely emergent in AFM-VBS lattice realizations. In contrast, the current QSH-SSC case has an exact U(1) symmetry at the Hamiltonian level corresponding to global charge conservation. This has important

consequences: skyrmions of the $\text{SO}(3)$ QSH order parameter carry charge $2e$ [9] and are therefore conserved. On the other hand, spinons corresponding to vortices of the SSC order parameter have spin-1/2 [9]. The thermodynamic and dynamical response of the system inside the quantum critical fan will be dominated by topology since charge and spin responses capture skyrmion and spinon degrees of freedom, respectively. In contrast to previous work on finite- T quantum criticality of AFM-VBS DQCPs [10–12], our fermionic approach allows us to characterize the topological excitations of the state inside the critical fan with susceptibilities of conserved quantities. Rather uniquely, it has gapless spin and charge excitations but a nonzero single-particle gap.

The remainder of the paper is organized as follows. The model is introduced in Sec. II, followed by a discussion of the methods used in Sec. III. Results are presented in Sec. IV and discussed in Sec. V. We provide an appendix on the scaling of conserved quantities.

II. MODEL

We consider the Hamiltonian [7]

$$\hat{H} = -t \sum_{\langle i,j \rangle} \left(\hat{c}_i^\dagger \hat{c}_j + \text{H.c.} \right) - \lambda \sum_{\square} \left(\sum_{\langle\langle i,j \rangle\rangle \in \square} \hat{J}_{i,j} \right)^2, \quad (1)$$

where $\hat{J}_{i,j} = i\nu_{ij}\hat{c}_i^\dagger\boldsymbol{\sigma}\hat{c}_j + \text{H.c.}$ We use the spinor notation $\hat{c}_i^\dagger = (\hat{c}_{i,\uparrow}^\dagger, \hat{c}_{i,\downarrow}^\dagger)$; $\hat{c}_{i,\sigma}^\dagger$ creates an electron at lattice site i on a honeycomb lattice (see also Fig. 1(a)) with physical spin σ . The first term in Eq. (1) accounts for nearest-neighbor hopping, the second term is a plaquette interaction involving next-nearest-neighbor pairs of sites and phase factors $\nu_{ij} = \pm 1$ identical to those of the Kane-Mele model [13]. The components of $\boldsymbol{\sigma} = (\sigma^x, \sigma^y, \sigma^z)$ are the Pauli spin-1/2 matrices. We consider half-filling and work in units where $\hbar = k_B = t = 1$.

Figure 1(b) shows the phase diagram. The $T = 0$ line was previously established in Refs. [7, 8]. The interaction is irrelevant for $\lambda < \lambda_{c1} = 0.0187(2)$, where the ground state is a Dirac semimetal (DSM). For $\lambda_{c1} < \lambda < \lambda_{c2} = 0.0332(2)$, the $\text{SU}(2)$ spin symmetry of Eq. (1) is spontaneously broken by long-range QSH order. For $\lambda > \lambda_{c2}$, the spin symmetry is restored and the QSH order gives way to the SSC with a spontaneously broken $\text{U}(1)$ symmetry. The DSM-QSHI transition exhibits fermionic Gross-Neveu-Heisenberg criticality [7, 8], whereas the QSHI-SSC transition appears to be described by the theory of DQCPs. Similar to AFM-VBS transitions in other fermionic models [14–16], the QSHI-SSC transition can be understood within a bosonic (single-fermion excitations being gapped) DQCP picture: the QSHI is destroyed by the proliferation of charge- $2e$ skyrmion defects in its order parameter whose condensation produces the

SSC [9]. At $T > 0$, long-range QSH order is prohibited by the Mermin-Wagner theorem, leading to a finite-temperature crossover (dashed line emerging from the DQCP in Fig. 1(b)). The SSC will be shown to undergo a Berezinskii-Kosterlitz-Thouless phase transition at $T_c(\lambda) > 0$ (solid line). The dashed lines in Fig. 1(b) provide an estimate of the range of the quantum critical region. The latter is not defined by a sharp transition line but by a crossover [1]. However, a temperature scale can be derived from the known scaling functions as well as the single-particle gap (for $\lambda < \lambda_{c2}$) and T_c (for $\lambda > \lambda_{c2}$), respectively (see Fig. 1 for details).

In the following, we focus on the couplings $\lambda = 0.026$ (QSHI), $\lambda = 0.0332$ (DQCP), and $\lambda = 0.050$ (SSC). As shown in Fig. 6 and discussed below, over this range, Hamiltonian (1) has a nonzero single-particle gap Δ_{sp} , which has important consequences for its symmetries. The generator of the model's $\text{SU}(2)$ spin symmetry is the total spin, $\hat{\mathbf{S}}_{\text{tot}} = \frac{1}{2} \sum_{i,\sigma,\sigma'} \hat{c}_{i,\sigma}^\dagger \boldsymbol{\sigma}_{\sigma\sigma'} \hat{c}_{i,\sigma'}$. Under a 2π rotation, $e^{2\pi i \mathbf{e} \cdot \hat{\mathbf{S}}_{\text{tot}}} = (-1)^{\hat{N}_{\text{tot}}}$, where $\hat{N}_{\text{tot}} = \sum_{i,\sigma} \hat{c}_{i,\sigma}^\dagger \hat{c}_{i,\sigma}$ corresponds to the total charge and \mathbf{e} is a unit vector in \mathbb{R}^3 . The nonzero gap pins the parity of the low-energy sector in which 2π rotations leave all quantities invariant. In other words, our model possesses a low-energy $\text{SO}(3) \times \text{U}(1)$ symmetry where $\text{U}(1)$ corresponds to charge conservation [17].

III. METHODS

The symmetry of Hamiltonian (1) under time reversal ensures the absence of a sign problem in our QMC simulations [7, 18].

To study finite-temperature properties, we used the ALF (Algorithms for Lattice Fermions) implementation [19] of the finite-temperature, auxiliary-field QMC method [20, 21]. We simulated lattices with $L \times L$ unit cells (each containing two orbitals) using a Trotter discretization $\Delta\tau = 0.2$ and periodic boundary conditions.

Results for dynamical quantities were obtained at $T = 0$ with the projective QMC algorithm from the ALF library [22]. This canonical algorithm filters out the ground state $|\psi_0\rangle$ from a trial wave function $|\psi_T\rangle$, required to be non-orthogonal to $|\psi_0\rangle$,

$$\frac{\langle\psi_0|\hat{O}|\psi_0\rangle}{\langle\psi_0|\psi_0\rangle} = \lim_{\Theta \rightarrow \infty} \frac{\langle\psi_T|e^{-\Theta\hat{H}}\hat{O}e^{-\Theta\hat{H}}|\psi_T\rangle}{\langle\psi_T|e^{-2\Theta\hat{H}}|\psi_T\rangle}. \quad (2)$$

We made the same choice for the Slater determinant for $|\psi_0\rangle$ as in Ref. [23], breaking lattice and point group symmetries but preserving time-reversal symmetry. Since $\lambda > 0$, we can decouple the interaction in Eq. (1) with a real-valued Hubbard-Stratonovich transformation. This makes both the imaginary-time propagation and the trial wave function invariant under time reversal. Consequently, the eigenvalues of the fermion matrix come in complex conjugate pairs and no sign problem arises.

We found a projection length $\Theta = L$ sufficient to converge to the finite-size ground state for the system sizes considered and used a symmetric Trotter decomposition to ensure Hermiticity of the imaginary time propagator; the Trotter time step was $\Delta\tau = 0.2$.

At $T = 0$, there is no distinction between particle, particle-hole and particle-particle channels. Accordingly, for an operator \hat{O}_q , the dynamical structure factor in the Lehmann representation takes the form

$$C^O(\mathbf{q}, \omega) \equiv \pi \sum_n |\langle \Psi_n | \hat{O}_q | \Psi_0 \rangle|^2 \delta(E_n - E_0 - \omega) \quad (3)$$

with $\hat{H}|\Psi_n\rangle = E_n|\Psi_n\rangle$. The QMC simulations yield correlators in imaginary time,

$$O(\mathbf{q}, \tau) = \langle \Psi_0 | \hat{O}_q^\dagger(\tau) \hat{O}_q | \Psi_0 \rangle, \quad (4)$$

which are related to the real-time observables by

$$O(\mathbf{q}, \tau) = \frac{1}{\pi} \int d\omega e^{-\tau\omega} O(\mathbf{q}, \omega). \quad (5)$$

The analytical continuation was done with the ALF implementation [22] of the stochastic maximum entropy method [24, 25].

IV. RESULTS

A. Finite-temperature properties

To investigate temperature effects, we computed the trace $\chi^\alpha(\mathbf{q}) = \text{tr} \chi_{\delta, \delta'}^\alpha(\mathbf{q})$ of the susceptibilities

$$\chi_{\delta, \delta'}^\alpha(\mathbf{q}) = \frac{1}{L^2} \sum_{\mathbf{r}, \mathbf{r}'} \int_0^\beta d\tau e^{i\mathbf{q} \cdot (\mathbf{r} - \mathbf{r}')} \langle \hat{O}_{\mathbf{r}, \delta}^\alpha(\tau) \hat{O}_{\mathbf{r}', \delta'}^\alpha(0) \rangle \quad (6)$$

for spin current operators

$$\hat{O}_{\mathbf{r}, \delta}^{\text{QSH}} = i\hat{c}_{\mathbf{r}}^\dagger \boldsymbol{\sigma} \hat{c}_{\mathbf{r}+\delta} + \text{H.c.} \quad (7)$$

and s-wave pairing operators

$$\hat{O}_{\mathbf{r}, \delta}^{\text{SSC}} = \frac{1}{2} \left(\hat{c}_{\mathbf{r}+\delta, \uparrow}^\dagger \hat{c}_{\mathbf{r}+\delta, \downarrow}^\dagger + \text{H.c.} \right). \quad (8)$$

Here, $\beta = 1/T$, \mathbf{r} corresponds to a hexagonal unit cell, $\mathbf{r} + \delta$ runs over all next-nearest neighbors, and $\mathbf{r} + \tilde{\delta}$ over the two orbitals of unit cell \mathbf{r} .

The QSHI and SSC are characterized by a divergence of the corresponding susceptibility $\chi^\alpha(\mathbf{q} = \mathbf{0})$. At $\lambda = 0.026$, $\chi^{\text{QSH}}(\mathbf{0})$ increases strongly with increasing L at low temperatures (Fig. 2(a)), whereas $\chi^{\text{SSC}}(\mathbf{0})$ saturates (Fig. 2(d)). Conversely, at $\lambda = 0.050$, $\chi^{\text{QSH}}(\mathbf{0})$ in Fig. 2(b) is essentially independent of L whereas $\chi^{\text{SSC}}(\mathbf{0})$ in Fig. 2(e) grows with increasing L at low T . A finite-size

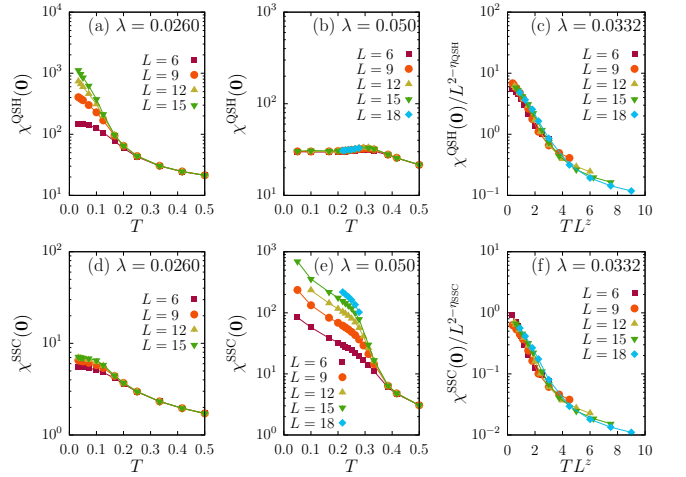


FIG. 2. (a)–(c) QSH and (d)–(f) SSC susceptibilities, revealing long-range QSH order at $T = 0$ for $\lambda = 0.026$ [(a), (d)] and s-wave superconductivity at $T < T_c$ for $\lambda = 0.050$ [(b), (e)]. Data collapse at the DQCP using $\lambda = \lambda_{c2} = 0.0332$, $\eta_{\text{QSH}} = 0.21$, $\eta_{\text{SSC}} = 0.22$, and $z = 1$ [(c), (f)].

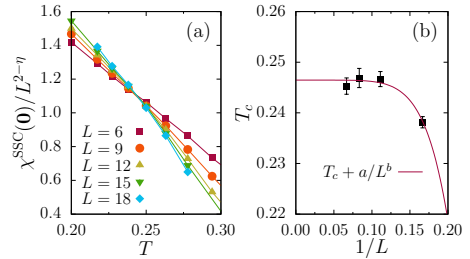


FIG. 3. (a) Scaling analysis of the SSC susceptibility using $\eta = 0.25$. (b) Extraction of T_c from finite-size extrapolation of the crossing points. Here, $\lambda = 0.050$ and $T_c = 0.0246(1)$.

scaling of $\chi^{\text{SSC}}(\mathbf{0})$ followed by an extrapolation of crossing points (Fig. 3) yields $T_c = 0.0246(1)$ for the SSC at $\lambda = 0.05$, the value shown in Fig. 1(b).

At criticality, and given Lorentz invariance [4, 10], we expect $\chi^\alpha(\mathbf{0}) = L^{(2-\eta^\alpha)} f(\beta/L)$ [26], consistent with the results for $\lambda = \lambda_{c2} = 0.0332$ in Figs. 2(c) and (f). Using the exponents $\eta_{\text{QSH}} = 0.21(5)$ and $\eta_{\text{SSC}} = 0.22(6)$ from Ref. [7], the data collapse has no free parameters.

Hamiltonian (1) has global $\text{SU}(2)$ spin and $\text{U}(1)$ charge symmetry. For conserved quantities, the uniform susceptibilities correspond to the fluctuations of the symmetry generators (here, $\hat{\mathbf{G}}^c = \hat{\mathbf{N}}_{\text{tot}}$, $\hat{\mathbf{G}}^s = \hat{\mathbf{S}}_{\text{tot}}$),

$$\chi^\alpha = \frac{\beta}{L^d} \left(\langle \hat{\mathbf{G}}^\alpha \cdot \hat{\mathbf{G}}^\alpha \rangle - \langle \hat{\mathbf{G}}^\alpha \rangle \cdot \langle \hat{\mathbf{G}}^\alpha \rangle \right). \quad (9)$$

In the QSHI, Fig. 4(a), χ^s scales to a finite value related to spin-wave excitations of the order parameter, whereas χ^c vanishes exponentially for $T \rightarrow 0$, reflecting insulating behavior. In the SSC, Fig. 4(b), spins are entangled in pairs, leading to an exponential decay of χ^s . At the same time, because a superconductor has no

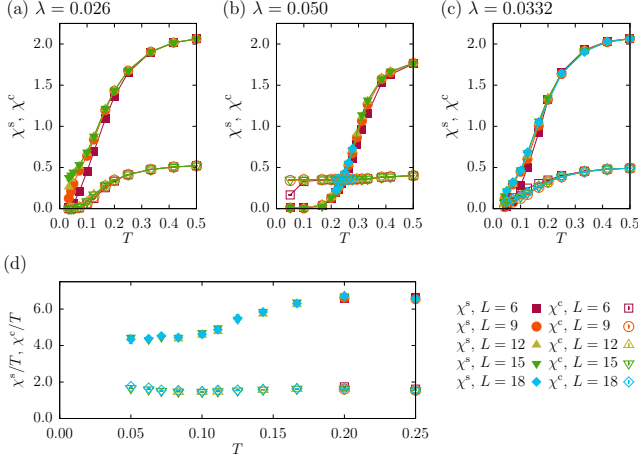


FIG. 4. (a)–(c) Temperature dependence of the uniform spin and charge susceptibilities. (d) Rescaled susceptibilities for selected parameters (see text), revealing linear behavior at low temperatures. The key applies to all panels.

gap for adding pairs, the corresponding charge susceptibility remains finite. At the critical point, Fig. 4(c), given a single length scale, susceptibilities of conserved quantities follow a hyper-scaling law. As shown in the Appendix, for $\beta = L^z$, $\chi \propto \beta^{1-d/z}$. Here, we have $d = 2$ and expect $z = 1$, which implies a linear temperature dependence of χ^s and χ^c . Retaining only size-converged data points—and keeping in mind potential, small deviations of $\lambda = 0.0332$ from the exact critical value λ_{c2} —the rescaled susceptibilities χ^s/T and χ^c/T in Fig. 4(d) approach a constant at low temperatures to acceptable accuracy, consistent with linear susceptibilities.

B. Dynamical properties

1. Single-particle excitations

Dynamical properties were calculated in an extended zone scheme in which \hat{O}_q for Eq. (4) is given by

$$\hat{c}_{q,\sigma} = \frac{1}{\sqrt{V}} \sum_{\mathbf{r}} e^{i\mathbf{q}\cdot\mathbf{r}} \left(\hat{a}_{\mathbf{r},\sigma} + \hat{b}_{\mathbf{r},\sigma} e^{i\mathbf{q}\cdot\mathbf{R}} \right) \quad (10)$$

with $\mathbf{R} = 2(\mathbf{a}_2 - \mathbf{a}_1)/3$. Here, \mathbf{r} runs over unit cells and $\hat{a}_{\mathbf{r},\sigma}$, $\hat{b}_{\mathbf{r},\sigma}$ are fermion annihilation operators of Wannier states centered around the A and B sites of the unit cell, as illustrated in Fig. 5(a).

Figure 6 shows the single-particle spectral function at $\lambda = 0.026$, $\lambda = 0.0332$, and $\lambda = 0.05$. As apparent, throughout the considered parameter range, the single-particle gap remains finite. As discussed in Sec. II, this leads to an emergent $\text{SO}(3) \times \text{U}(1)$ symmetry, corresponding to rotations in spin space and charge conservation, respectively. Since the QSH order corresponds to a Dirac mass, the single-particle gap in the vicinity of

the DSM-QSH transition opens at the Dirac point, K. At $\lambda = 0.026$, we see that the gap is indeed determined by the Dirac point. However, upon increasing λ , the position of the minimal gap changes from the Dirac point K to the M point.

The $T = 0$ single-particle gap Δ_{sp} —defined as the minimal energy for single-particle excitations—can be extracted by fitting the tail of the single-particle Green function at the corresponding wave vector (K for $\lambda = 0.026$, M for $\lambda = 0.0332$ and 0.05) to a single exponential. The finite-size extrapolation shown in Fig. 6(d) reveals that the gap remains nonzero in the thermodynamic limit. These results are qualitatively consistent with those obtained previously using a projective QMC method [7], although in the former work Δ_{sp} was determined at K for all values of λ .

2. QSH and SSC dynamical correlations

In Fig. 7, we present the $T = 0$ dynamic structure factors of the QSHI and SSC order parameters ($\alpha = \text{QSH, SSC}$),

$$C^\alpha(\mathbf{q}, \omega) = \pi \sum_n |\langle \Psi_n | \hat{O}_q^\alpha | \Psi_0 \rangle|^2 \delta(E_n - E_0 - \omega), \quad (11)$$

again calculated in the extended zone scheme.

The superconducting order parameter is a local quantity. Therefore, the definition of \hat{O}_q in Eq. (3) is not ambiguous, see also Fig. 5(a), and reads

$$\hat{O}_q^{\text{SSC}} = \frac{1}{\sqrt{V}} \sum_{\mathbf{r}} e^{i\mathbf{q}\cdot\mathbf{r}} \left(\text{Re} \left[\hat{a}_{\mathbf{r},\uparrow}^\dagger \hat{a}_{\mathbf{r},\downarrow}^\dagger \right] + \text{Re} \left[\hat{b}_{\mathbf{r},\uparrow}^\dagger \hat{b}_{\mathbf{r},\downarrow}^\dagger \right] e^{i\mathbf{q}\cdot\mathbf{R}} \right). \quad (12)$$

In contrast, the QSH operator resides on links and we have used the mid-point of the link to define the Fourier transform in the extended zone scheme:

$$\hat{O}_q^{\text{QSH}} = \frac{1}{\sqrt{V}} \sum_{\mathbf{r}} e^{i\mathbf{q}\cdot\mathbf{r}} \sum_{\delta=1}^6 \hat{O}_{\mathbf{r},\delta}^{\text{QSH}} e^{i\mathbf{q}\cdot\mathbf{R}_\delta}. \quad (13)$$

Here, \mathbf{r} corresponds to the center of the hexagon (there is a one-to-one mapping between unit cell coordinates and the center of the hexagons). As shown in Fig. 5(b), $\mathbf{R}_1 = (\mathbf{a}_2/2 - \mathbf{a}_1)/3$, $\mathbf{R}_2 = (\mathbf{a}_2 - \mathbf{a}_1)/3$, $\mathbf{R}_3 = (\mathbf{a}_2 + \mathbf{a}_1)/6$, $\mathbf{R}_4 = -(\mathbf{a}_2/2 - \mathbf{a}_1)/3$, $\mathbf{R}_5 = -(\mathbf{a}_2 - \mathbf{a}_1)/3$, $\mathbf{R}_6 = -(\mathbf{a}_2 + \mathbf{a}_1)/6$.

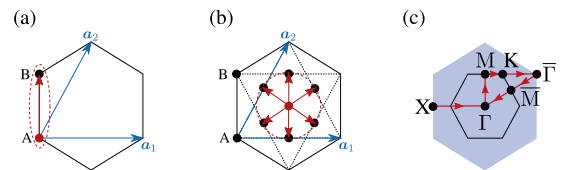


FIG. 5. Notation used in the context of the extended zone scheme and illustration for (a) local operators and (b) nonlocal QSH operators. (c) Path in the Brillouin zone.

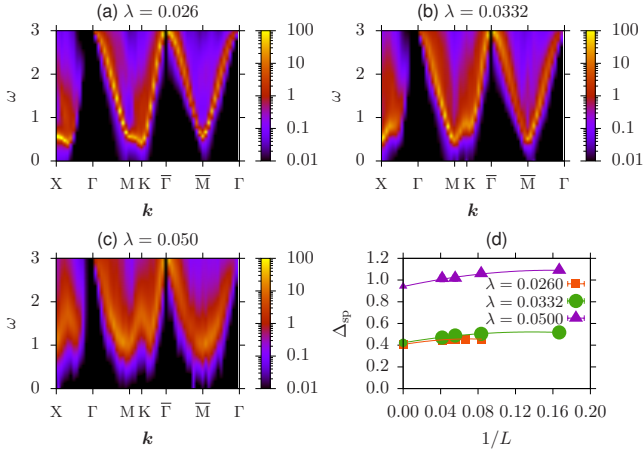


FIG. 6. (a)–(c) $T = 0$ single-particle spectral function for $L = 24$. (d) Finite-size scaling of the single-particle gap. The path in the Brillouin zone is shown in Fig. 5(c).

In the QSHI, the $\text{SO}(3)$ symmetry is spontaneously broken, as apparent from the low-lying Goldstone modes at the Γ points in Fig. 7(a). Skyrmions of the $\text{SO}(3)$ order parameter carry charge $2e$, $\rho(\mathbf{r}) = \frac{2e}{4\pi} \mathbf{N}(\mathbf{r}) \cdot \partial_x \mathbf{N}(\mathbf{r}) \times \partial_y \mathbf{N}(\mathbf{r})$, where $\mathbf{N}(\mathbf{r})$ is the normalized QSH order parameter [9]. Therefore, adding an s-wave pair to the system corresponds to a skyrmion addition process or, equivalently, a monopole. Given their charge $2e$ and the charge-conserving QSH order parameter, the skyrmions' dynamics is revealed by $C^{\text{SSC}}(\mathbf{q}, \omega)$ (Fig. 7(b)) and indicates that they are massive in the QSHI. The gap to the first skyrmion excitation is smaller than twice the single-particle gap ($2\Delta_{\text{sp}} \approx 0.8$), thereby confirming that they are the elementary charge excitations for $\lambda = 0.026$.

The SSC spontaneously breaks a $\text{U}(1)$ symmetry and is hence also characterized by Goldstone modes, as visible in Fig. 7(d) at the Γ points. Our understanding is that the SSC is the result of skyrmion condensation. A distinct feature of this state is that the vortex of the $\text{U}(1)$ order parameter carries a spin-1/2 degree of freedom [9], a spinon. Pairs of spinons transform as an $\text{SO}(3)$ vector and can be observed in $C^{\text{QSH}}(\mathbf{q}, \omega)$. In fact, even for $\lambda = 0.05$, very far from the critical point, $C^{\text{QSH}}(\mathbf{q}, \omega)$ shows states well below the particle-hole continuum at $2\Delta_{\text{sp}} \approx 1.9$ (Fig. 7(c)). We interpret this as a signature of the gapped two-spinon continuum of the SSC.

3. Spin and charge dynamics

For the spin dynamics, $C^S(\mathbf{q}, \omega) \equiv S(\mathbf{q}, \omega)$, the operator $\hat{O}_{\mathbf{q}}$ in Eq. (3) corresponds to the vector

$$\hat{S}_{\mathbf{q}} = \frac{1}{\sqrt{V}} \sum_{\mathbf{r}} e^{i\mathbf{q} \cdot \mathbf{r}} \frac{1}{2} (\mathbf{a}_{\mathbf{r}}^{\dagger} \boldsymbol{\sigma} \mathbf{a}_{\mathbf{r}} + \mathbf{b}_{\mathbf{r}}^{\dagger} \boldsymbol{\sigma} \mathbf{b}_{\mathbf{r}} e^{i\mathbf{q} \cdot \mathbf{R}}) \quad (14)$$

where we have adopted the same notation as in Eq. (10); $\boldsymbol{\sigma}$ is a vector of Pauli spin matrices and $\mathbf{a}_{\mathbf{r}}^{\dagger} = (a_{\mathbf{r},\uparrow}^{\dagger}, a_{\mathbf{r},\downarrow}^{\dagger})$.

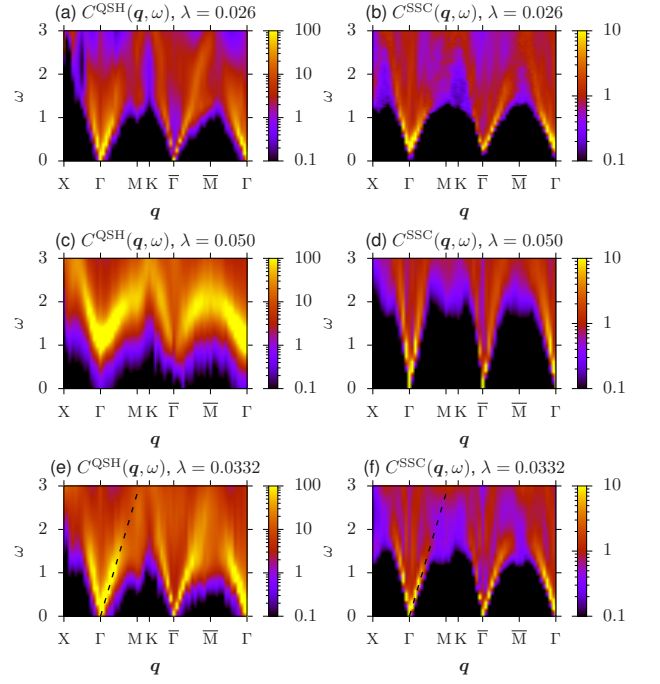


FIG. 7. Zero-temperature dynamical QSH [(a),(c),(e)] and s-wave pairing [(b),(d),(f)] structure factors at different values of λ for $L = 24$. The dashed lines in (e) and (f) correspond to $\omega = a(\mathbf{q} - \Gamma)$ with the same a . The path in the Brillouin zone is shown in Fig. 5(c).

For the charge dynamics, $C^N(\mathbf{q}, \omega) \equiv N(\mathbf{q}, \omega)$, $\hat{O}_{\mathbf{q}}$ in Eq. (3) corresponds to

$$\hat{N}_{\mathbf{q}} = \frac{1}{\sqrt{V}} \sum_{\mathbf{r}} e^{i\mathbf{q} \cdot \mathbf{r}} (\mathbf{a}_{\mathbf{r}}^{\dagger} \mathbf{a}_{\mathbf{r}} + \mathbf{b}_{\mathbf{r}}^{\dagger} \mathbf{b}_{\mathbf{r}} e^{i\mathbf{q} \cdot \mathbf{R}}). \quad (15)$$

The spin and charge dynamic structure factors at $\lambda = 0.026$, $\lambda = 0.0332$, and $\lambda = 0.05$ are shown in Fig. 8. The spin operator transforms like the QSH order parameter under $\text{SU}(2)$ rotations so that both quantities probe spin excitations. Similarly, both the superconducting order parameter and the charge operator probe charge fluctuations. We hence expect to see similarities between the dynamical QSH (SSC) and dynamical spin (charge) structure factors. Aside from differences in spectral weight, and accounting for uncertainties related to the analytical continuation, this is indeed borne out by the results in Figs. 7 and 8. In particular, $S(\mathbf{q}, \omega)$ ($N(\mathbf{q}, \omega)$) shows gapless (gapped) modes in the QSH phase, Figs. 8(a),(b), whereas the behavior is reversed in the SSC, see Figs. 8(e),(f). At criticality, Figs. 8(c),(d), both charge and spin dynamical responses show very similar low-energy features. As pointed out in the main text, this reflects an emergent $\text{SO}(5)$ symmetry.

At $\mathbf{q} = \mathbf{0}$ (i.e., at Γ and $\bar{\Gamma}$) the spectral weight is expected to vanish because the structure factor probes the total spin and total charge fluctuations. These quantities correspond to the generators of the spin and charge symmetries and vanish identically at zero temperature.

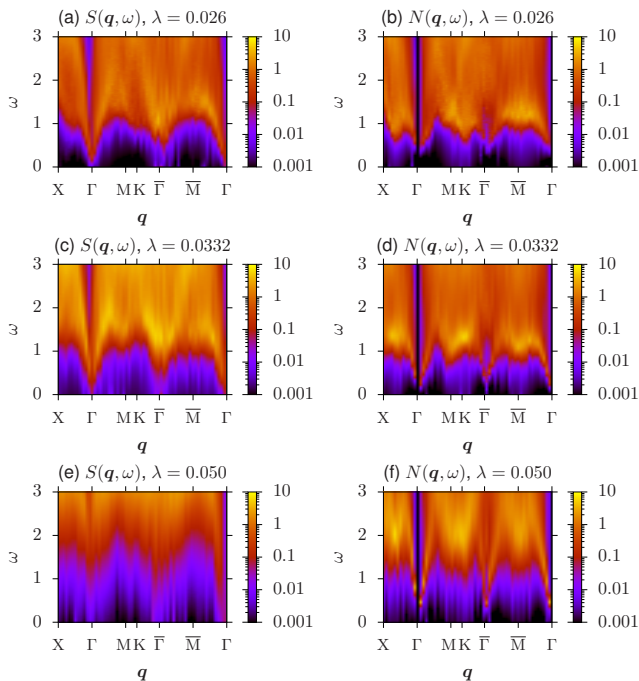


FIG. 8. Zero-temperature spin [(a),(c),(e)] and charge dynamic structure factors [(b),(d),(f)] for $L = 24$. The path in the Brillouin zone is shown in Fig. 5(c)

In our QMC simulations, the $SU(2)$ spin symmetry is restored only after the sampling (and, strictly speaking, in the limit $\Delta\tau \rightarrow 0$), so that the above statement is valid only within error bars. On the other hand, the charge is conserved for each Hubbard-Stratonovich configuration. This provides an explanation for why $N(\mathbf{0}, \omega) \equiv 0$ whereas $S(\mathbf{0}, \omega)$ is small but finite.

Based on the above discussion, we expect the DQCP to be characterized by gapless spin-1/2 spinons and gapless charge-2e skyrmions. This is confirmed by Figs. 7(e) and (f). Note that at criticality, the particle-hole continuum is located at $2\Delta_{sp} \approx 0.8$. The gapless spin and charge excitations lead to the observed linear temperature scaling of the charge and spin susceptibilities. The remarkable similarity of the QSH and SSC dynamical structure factors below the particle-hole continuum, most notably the identical velocities of excitations indicated by the dashed lines, can be understood in terms of an emergent Lorentz symmetry that implies the existence of a single velocity, the velocity of light.

V. DISCUSSION

Hamiltonian (1) provides a realization of a DQCP between a QSHI and an SSC. The quantum critical region shown in Fig. 1(b) has distinct thermodynamic and dynamical signatures: the single-particle gap is finite but the spin and charge susceptibilities reveal gapless excitations in the respective channels. Gapless charge excita-

tions capture skyrmions of the $SO(3)$ QSH order parameter with charge $2e$. Gapless spin excitations reflect the vortices of the $U(1)$ SSC order parameter with spin-1/2. A natural upper bound for the quantum critical region is the single-particle gap. Below this energy scale, the very symmetry of the quantum critical theory emerges. In fact, the generation of quantum anomalies by gapping out fermions has been put forward in Ref. [17], where it is conjectured that the state at λ_{c2} is an intrinsically gapless topological state.

The interpretation of the data proposed above naturally emerges when describing the DQCP in terms of a five component non-linear sigma model with $SO(3) \times U(1)$ symmetry subject to a Wess-Zumino-Witten term [9, 27–29]. This field theory is derived perturbatively from Dirac fermions subject to a Yukawa coupling to the five anticommuting QSH and SSC mass terms [30] by integrating out the gapped fermionic degrees of freedom. There is evidence of an emergent $SO(5)$ symmetry at intermediate energy scales [31, 32]. In particular, the anomalous dimensions of the QSH and SSC order parameters are equal within error bars [7]. It should be noted that, at the energy scales set by our finite lattice sizes, we cannot distinguish between weakly first-order transitions—characterized by the proximity to a critical point with $SO(5)$ symmetry [33, 34]—and genuine second-order phase transition. The proximity to an $SO(5)$ critical point is consistent with our spectra and the symmetry implies identical supports for the QSH and SSC dynamical structure factors at criticality.

The transition to the SSC at T_c is particularly interesting close to the DQCP at energy scales well below the single-particle gap. At T_c , vortices of the SSC order parameter unbind. Since they carry a spin-1/2 degree of freedom, the resulting state above T_c should be understood as a liquid of spinons. Within the theory of the DQCP [3, 4], this gas of spinons is described by a non-compact CP^1 field theory in its deconfined phase. The spinons are captured by the spin susceptibility whereas the charge susceptibility reveals the gauge-field flux corresponding to the charged skyrmions. Remarkably, the nontrivial vortex core does not seem to impact the temperature-driven transition to the normal phase. Instead, the finite-size scaling analysis underlying the determination of T_c yields a clean crossing point when assuming the usual 2D XY exponents, see Fig. 3(a).

The QSHI-SSC DQCP considered differs in important aspects from AFM-VBS DQCPs in JQ [35] or loop models [36]. The JQ model has a second length scale associated with the energy scale where the emergent $U(1)$ symmetry gives way to the C_4 point group symmetry of the Hamiltonian. This implies that the uniform spin susceptibility does not scale linearly with T at criticality, as confirmed numerically [37].

Recently, doping of the QSH state at $\lambda = 0.026$ and $T = 0$ was shown to yield a continuous and direct transition to an SSC [23]. The thermodynamic and dynamical properties of this transition are of particular interest for

future work. The spectra in Fig. 7 reveal the existence of preformed pairs identified here as skyrmions. The study of thermodynamic quantities at finite doping could hence reveal pseudogap physics extensively discussed in connection with high-temperature superconductivity.

ACKNOWLEDGMENTS

We thank Chong Wang for helpful discussions. The authors gratefully acknowledge the Gauss Centre for Supercomputing e.V. (www.gauss-centre.eu) for funding this project by providing computing time on the GCS Supercomputer SUPERMUC-NG at the Leibniz Supercomputing Centre (www.lrz.de). TS thanks the Deutsche Forschungsgemeinschaft (DFG) for funding via grant SA 3986/1-1. FFA thanks the DFG for funding via grant AS 120/15-1 and the Würzburg-Dresden Cluster of Excellence on Complexity and Topology in Quantum Matter ct.qmat (EXC 2147, project-id 390858490). MH and ZW acknowledge support from the DFG via SFB 1170 ToCoTronics. YL was supported by the China Postdoctoral Science Foundation under grants no. 2019M660432 and 2020T130046 as well as the National Natural Science Foundation of China under grants no. 11947232 and U1930402. WG was supported by the National Natural Science Foundation of China under grants no. 12175015 and 11734002.

Appendix: Scaling of conserved quantities

We consider a Hamiltonian $\hat{H} = \sum_i K_i \hat{O}_i$ that commutes with the generator of a global symmetry, \hat{G} . In our specific case, \hat{G} corresponds either to the total particle number or to a component of the total spin. The partition function is block diagonal in \hat{G} ,

$$Z(\mathbf{K}, L, \beta, \mu, l) \equiv \text{Tr} e^{-\beta(\hat{H} - \mu \hat{G})} \quad (\text{A.1})$$

$$= \sum_G e^{\beta \mu G} Z_G(\mathbf{K}, L, \beta, l). \quad (\text{A.2})$$

Here, μ corresponds to a Lagrange multiplier, L is the linear length of the system, β the inverse temperature, l an additional length scale and Z_G the partition function in the Hilbert space spanned by the vectors $\hat{G}|\Psi\rangle = G|\Psi\rangle$. We note that the additional length scale also diverges at the critical point, albeit with a distinct exponent. The

susceptibility reads

$$\chi_G = - \left. \frac{\partial^2 f}{\partial \mu^2} \right|_{\mu=0} = \frac{\beta}{L^d} (\langle \hat{G}^2 \rangle - \langle \hat{G} \rangle^2), \quad (\text{A.3})$$

where $f = -\frac{1}{\beta L^d} \log Z$ is the free-energy density and $\langle \hat{O} \rangle = \frac{1}{Z} \text{Tr} [e^{-\beta \hat{H}} \hat{O}]$. We carry out a renormalization group (RG) transformation in each G sector:

$$Z_G(\mathbf{K}, L, \beta, l) = Z_G \left(\mathbf{K}^{(1)}, \frac{L}{b}, \frac{\beta}{b^z}, \frac{l}{b^{z_l}} \right). \quad (\text{A.4})$$

Here, z corresponds to the dynamical critical exponent and z_l encodes the presence of an additional length scale. The RG transformations of the couplings \mathbf{K} and the exponents do not depend on G . This can be justified as follows. Consider a situation where there is a gap between the G sector corresponding to $\mu = 0$ and all other sectors. Then, fluctuations of G are exponentially suppressed as a function of temperature and it is meaningful to consider a single G sector. In this case, χ_G vanishes exponentially and hence exhibits no scaling behavior. Let us now consider the more interesting case where there is no gap in the G spectrum. In this case, we expect that $\sqrt{\langle \hat{G}^2 \rangle - \langle \hat{G} \rangle^2} / \langle \hat{G} \rangle$ vanishes in the thermodynamic limit.

We note that for, say, \hat{G} corresponding to the total particle number, the vanishing of the latter relation implies that the particle number is sharp in the grand canonical ensemble so that the canonical and grand canonical ensembles are equivalent in the thermodynamic limit. The same argument holds for the equivalence of the canonical and micro-canonical ensembles. Hence in the absence of a gap, G is still *sharp*, in the above sense, so that an RG flow independent of G is validated.

With this in mind, we can apply the RG transformation to the susceptibility and obtain:

$$\chi_G(\mathbf{K}, L, \beta, \mu, l) = \frac{b^z}{b^d} \chi_G \left(\mathbf{K}^{(1)}, \frac{L}{b}, \frac{\beta}{b^z}, \frac{l}{b^{z_l}} \right). \quad (\text{A.5})$$

Let us now iterate the RG transformation n times, place ourselves at the critical point, $\mathbf{K}^{(1)} = \mathbf{K} = \mathbf{K}^*$, set $b^n = L$, $\beta = L^z$ to get

$$\chi_G(\mathbf{K}^*, L, \beta, l) = \beta^{1-\frac{d}{z}} \chi_G \left(\mathbf{K}^*, \frac{l}{L^{z_l}} \right) = \beta^{1-\frac{d}{z}} f \left(\frac{l^{1/z_l}}{L} \right). \quad (\text{A.6})$$

Hence, in the absence of a second length scale, $z_l = 1$, we conclude that $\chi_G(\mathbf{K}^*, L, \beta, l) \propto \beta^{1-d/z}$. Given a second length scale, corrections to this scaling law are expected.

* These authors contributed equally to this work and are listed alphabetically.

† fakher.assaad@physik.uni-wuerzburg.de

1 S. Sachdev, *Quantum Phase Transitions* (Cambridge Uni-

versity Press, 2011).

2 P. Gegenwart, Q. Si, and F. Steglich, *Nature Physics* **4**, 186 (2008).

3 T. Senthil, L. Balents, S. Sachdev, A. Vishwanath, and

- M. P. A. Fisher, Phys. Rev. B **70**, 144407 (2004).
- ⁴ T. Senthil, A. Vishwanath, L. Balents, S. Sachdev, and M. P. A. Fisher, Science **303**, 1490 (2004).
 - ⁵ X. Y. Xu, Y. Qi, L. Zhang, F. F. Assaad, C. Xu, and Z. Y. Meng, Phys. Rev. X **9**, 021022 (2019).
 - ⁶ A. M. Polyakov, *Gauge Fields and Strings* (Routledge, 2018).
 - ⁷ Y. Liu, Z. Wang, T. Sato, M. Hohenadler, C. Wang, W. Guo, and F. F. Assaad, Nature Communications **10**, 2658 (2019).
 - ⁸ Y. Liu, Z. Wang, T. Sato, W. Guo, and F. F. Assaad, Phys. Rev. B **104**, 035107 (2021).
 - ⁹ T. Grover and T. Senthil, Phys. Rev. Lett. **100**, 156804 (2008).
 - ¹⁰ R. G. Melko and R. K. Kaul, Phys. Rev. Lett. **100**, 017203 (2008).
 - ¹¹ A. W. Sandvik, V. N. Kotov, and O. P. Sushkov, Phys. Rev. Lett. **106**, 207203 (2011).
 - ¹² S. Jin and A. W. Sandvik, Phys. Rev. B **87**, 180404 (2013).
 - ¹³ C. L. Kane and E. J. Mele, Phys. Rev. Lett. **95**, 146802 (2005).
 - ¹⁴ T. Sato, M. Hohenadler, and F. F. Assaad, Phys. Rev. Lett. **119**, 197203 (2017).
 - ¹⁵ Z.-X. Li, Y.-F. Jiang, S.-K. Jian, and H. Yao, Nature Communications **8**, 314 (2017).
 - ¹⁶ X. Y. Xu, K. T. Law, and P. A. Lee, Phys. Rev. B **98**, 121406 (2018).
 - ¹⁷ R. Thorngren, A. Vishwanath, and R. Verresen, Phys. Rev. B **104**, 075132 (2021).
 - ¹⁸ C. Wu and S.-C. Zhang, Phys. Rev. B **71**, 155115 (2005).
 - ¹⁹ M. Bercx, F. Goth, J. S. Hofmann, and F. F. Assaad, SciPost Phys. **3**, 013 (2017).
 - ²⁰ R. Blankenbecler, D. J. Scalapino, and R. L. Sugar, Phys. Rev. D **24**, 2278 (1981).
 - ²¹ F. Assaad and H. Evertz, in *Computational Many-Particle Physics*, Lecture Notes in Physics, Vol. 739, edited by H. Fehske, R. Schneider, and A. Weiße (Springer, Berlin Heidelberg, 2008) pp. 277–356.
 - ²² ALF Collaboration, F. F. Assaad, M. Bercx, F. Goth, A. Götz, J. S. Hofmann, E. Huffman, Z. Liu, F. P. Toldin, J. S. E. Portela, and J. Schwab, (2021), arXiv:2012.11914 [cond-mat.str-el].
 - ²³ Z. Wang, Y. Liu, T. Sato, M. Hohenadler, C. Wang, W. Guo, and F. F. Assaad, Phys. Rev. Lett. **126**, 205701 (2021).
 - ²⁴ A. Sandvik, Phys. Rev. B **57**, 10287 (1998).
 - ²⁵ K. S. D. Beach, (2004), cond-mat/0403055.
 - ²⁶ M. Campostrini, A. Pelissetto, and E. Vicari, Phys. Rev. B **89**, 094516 (2014).
 - ²⁷ A. Tanaka and X. Hu, Phys. Rev. Lett. **95**, 036402 (2005).
 - ²⁸ A. Abanov and P. Wiegmann, Nuclear Physics B **570**, 685 (2000).
 - ²⁹ T. Senthil and M. P. A. Fisher, Phys. Rev. B **74**, 064405 (2006).
 - ³⁰ S. Ryu, C. Mudry, C.-Y. Hou, and C. Chamon, Phys. Rev. B **80**, 205319 (2009).
 - ³¹ A. Nahum, P. Serna, J. T. Chalker, M. Ortuño, and A. M. Somoza, Phys. Rev. Lett. **115**, 267203 (2015).
 - ³² Z. Wang, M. P. Zaletel, R. S. K. Mong, and F. F. Assaad, Phys. Rev. Lett. **126**, 045701 (2021).
 - ³³ R. Ma and C. Wang, Phys. Rev. B **102**, 020407 (2020).
 - ³⁴ A. Nahum, Phys. Rev. B **102**, 201116 (2020).
 - ³⁵ A. W. Sandvik, Phys. Rev. Lett. **98**, 227202 (2007).
 - ³⁶ A. Nahum, J. T. Chalker, P. Serna, M. Ortuño, and A. M. Somoza, Phys. Rev. X **5**, 041048 (2015).
 - ³⁷ H. Shao, W. Guo, and A. W. Sandvik, Science **352**, 213 (2016).